Sensors and Actuators A 329 (2021) 112825

Contents lists available at ScienceDirect

Sensors and Actuators A: Physical

journal homepage: www.elsevier.com/locate/sna

# Current sensor optimization based on simulated transfer function under partial discharge pulses☆

Douglas Nascimento[a,b], Shady S. Refaat[c], Hermes Loschi[a,b,d,*], Yuzo Iano[e], Euclides Chuma[e], Waseem El-Sayed[a,b], Amr Madi[a,b]

[a] Faculty of Computer, Electrical and Control Engineering, University of Zielona Gora, Zielona Gora, Poland
[b] Faculty of Electrical Engineering, Mathematics and Computer Science (EEMCS), University of Twente, Enschede, Netherlands
[c] Electrical and Computer Engineering Department, Texas A&M University at Qatar, Doha, Qatar
[d] Department of Electrical and Electronic Engineering, University of Nottingham, Nottingham, United Kingdom
[e] School of Electrical and Computer Engineering, University of Campinas, São Paulo, Brazil

ARTICLE INFO

*Article history:*
Received 19 November 2020
Received in revised form 23 April 2021
Accepted 7 May 2021
Available online 11 May 2021

*Keywords:*
High-frequency current transformer
Partial discharges
Sensor modelling
Physical effects

ABSTRACT

The time measurement efficiency of the partial discharge (PD) relies on the signal-to-noise ratio (SNR) and gain of the high-frequency current transformer (HFCT) sensor. However, the PD's time measurement efficiency decreases with the noise coupled to the HFCT in onsite measurements. To overcome that setback, this paper proposes one pre-processing, through modelling and simulation, considering the physical effects, features of the electrical circuit and coil construction parameters of the HFCT. The main goal is to reach reasonable high SNR under the strong influence of background noises. This investigation aims to validate the hypothesis of improvement or deterioration of the HFCT signal response through a transfer function optimization. This research effort's contributions are threefold: 1. Generation of PD pulse signal and noise addition; 2. HFCT modelling, simulation, and frequency response analysis; and 3. Models performance evaluation and validation of hypothesis. In conclusion, the pre-processing approach stands out as a means to robustify and provide freedom to the electric utility, making up for an eventual need to redefine the physical and geometrical parameters of the HFCT sensor under specific background noise for maintenance tests purpose. According to a cyber-physical system framework, experiments corroborate the project's goals to contribute to the PD pattern monitoring in onsite measurements and incorporate robustness to signals with low SNRs.



## 1. Introduction

The dielectric material degradation in electrical systems is generally associated with the partial discharges (PD) [1], unleashed within voids, and cracks in conductor–dielectric interfaces in solid insulation systems (bubbles), in the case of liquid dielectrics or corona, in gaseous [2]. Under the electric insulation system's operating stress conditions, the voltage across the damaged insulation, within bubbles, cracks, voids, may exceed its dielectric strength leading to electric discharges in the dielectric, reducing the stiffness and finally leading to total or partial failure of the insulation [3].

Thus, it is recommended to make quality and compliance tests by PD analysis. Also, considering cyber-physical system frameworks (e.g. [4]), the analysis of PD can be extrapolated as an redundant component of power systems on alerting the active agents (electrical utilities, stakeholders, power system companies) in advance when any component it is about to collapse due to PD. The PD tests are classified according to the measuring technique, and electric methods are widely used [1]. Electrical methods can be performed on high voltage electrical equipment such as power transformers, instrument transformers, medium, high and extra-high voltage cables, high voltage bushings and rotary machines [5]. Furthermore, the electrical methods are divided into conventional and non-conventional. Conventional PD methods are performed following IEC 60270 - High Voltage testing techniques: Partial Dis-

☆ This publication was made possible by the University of Twente. The statements made herein are solely the responsibility of the author.
* Corresponding author.
*E-mail addresses:* eng.douglas.a@ieee.org (D. Nascimento), shady.khalil@qatar.tamu.edu (S.S. Refaat), eng.hermes.loschi@ieee.org (H. Loschi), yuzo@decom.fee.unicamp.br (Y. Iano), euclides.chuma@ieee.org (E. Chuma), waseem.elsayed@ieee.org (W. El-Sayed), amr.madi@ieee.org (A. Madi).
*URLs:* http://www.uz.zgora.pl (D. Nascimento), http://www.loschihermes.com (H. Loschi).

https://doi.org/10.1016/j.sna.2021.112825

charge measuring techniques [6], using a coupling capacitor with a central measuring frequency of up to 1 MHz. On the other hand, non-conventional PD methods (or electromagnetic methods [7]) are based on IEC 62478 - High Voltage testing techniques - measurement of Partial Discharge by Electromagnetic and Acoustic methods [8], which employ sensors that operate in frequencies in the range comprising: High Frequency - HF (3-30 MHZ), VHF - Very High Frequency (30 - 300 MHz) and Ultra High Frequency - UHF (300 MHz - 3 GHz) [9]. In HF, among the widely used sensors for PD measuring through the inductive coupling of electric current is the High Frequency Current Transformer (HFCT) [7].

The time measurement efficiency of the PD relies on the signal-to-noise (SNR) ratio and gain of the HFCT sensor. However, the PD's time measurement efficiency decrease with the noise coupled to the HFCT in onsite measurements. Traditionally, the PD measurement approach considers the noise removal using mathematical algorithms and efficient software in the time and frequency domain, such as spectral subtraction denoising (SSD), discrete wavelet transform (DWT), wavelet shrinkage denoising (WSD), Principal Component Analysis (PCA) [10,11], and Complex Daubechies Wavelet (CDW) [12,13]. Overall, enabling the correct understanding of the PD phenomenon magnitude in onsite measurements.

However, this paper aims to validate the hypothesis of improvement or deterioration of the HFCT signal response, through a transfer function optimization, for an eventual redefinition of physical and geometrical parameters of the HFCT sensor. Thus, through the investigation of the physical effects, modelling, and simulation of the HFCT, applied to time measurements of the PD under the strong influence of background noises, expected to reach reasonable higher SNR. Therefore, the methodology proposed in this paper goes beyond a traditional sensor optimization approach [14]. It's considered HFCT's optimization and on-field emulation tasks to the PD measurements by implementing additive white Gaussian noise (AWGN) miscellaneous.

The proposed methodology was divided and developed linearly based on three steps as shown in Fig. 1: 1. PD pulse generation and noise addition; 2. Modelling of the HFCT sensor; and 3. Performance evaluation. Step 1 comprises the PD signal generation, modeled by traveling waves method [15] and application of characteristic background noise through AWGN to the signal generated [1]. In step 2, HFCT sensor modelling was performed, based on the Electromagnetism Laws, according to [16], whereas the frequency responses were carried out based on [14]. In step 3, HFCT models were created based on the variation of constructive and electrical parameters and subsequent evaluation of TFs (Transfer Functions) performance [12]. In Fig. 1 $s(i)$ represents the PD input signal, $r(i)$ denotes noise (AWGN), $Z(i)$ means the TFs of the HFCT models ($g(s)$) under analysis and, $i$ is the discrete time index.

Traditionally, the design process of a sensor uses statistical operators customarily applied as the last evaluation step, i.e., step 3 of Fig. 1. The main goal of statistical operators is to evaluate the sensor response performance regarding the similarity and prediction quality. It is done by comparing the output "pre-processed" signal from the sensor and the exact input signal (in this paper, PD pulse) [12,13,17,18]. Therefore in this paper, the HFCT sensor performance was evaluated by mean squared error (MSE) and cross-relation (XCORR). An optimal response near zero is expected for MSE and one for XCORR, considering the normalization. Thereby, the prediction and similarity of HFCT sensor performance drive the decision on which is the best model, both in terms of electrical and geometrical parameters, i.e., the best fitted HFCT sensor model.

The rest of this paper is organized as follows. Section 2 addresses the PD mechanisms, its generation, and noise addition, and in Section 3 is explained the HFCT modelling and simulation. Section 4 evaluate the HFCT performance by MSE and XCORR. Finally, concluding remarks are provided in Section 5.

## 2. PD mechanisms

PD are characterized by electrical pulses of current within the insulation system of the device under test (DUT), proportional to a load of the current pulse at the input of the circuit. Fig. 2 shows the online measuring of PD by using HFCT. The quantities related to the PD pulses are established in standard [6], e.g. apparent load ($q$), pulse repetition rate ($n$), phase angle ($\phi$) and time ($t$) of pulse occurrence.

The representation of PD signals is conducted through three categories of standards [19]: 1. resolved phase data, such as the $\phi - q - n$ diagram (Fig. 2a.); 2. resolved time data, i.e. $q - t$ waveform – where $q$ is the load magnitude and $t$ the analysis interval, or $V - t$ – where $V$ represents the voltage over time $t$; 3. signal data that are neither resolved phase nor resolved time, e.g. the $q - V$ diagram – magnitude variation of discharge pulse by test voltage amplitude or the Pulse Sequence Analysis (PSA) diagram – in that data related to PD pulses should be saved as a sequence [3].

### 2.1. PD pulse

The characteristics of PD current pulse are analyzed using parameters rise time ($T_r$), pulse width ($T_w$) and fall time ($T_f$). All the PD current pulses are from the origin time $t_0$ of the voltage step, which refers to the time when the increasing voltage has 10% of initial voltage ($V_0$). That is, $T_r$ regards the time interval between 10% and 90% of the pulse amplitude, $T_f$ is the time interval between 90% and 10% of the pulse amplitude, and $T_w$ is the time interval between 50% of the rising signal and 50% of the fall signal, pulse height, and maximum pulse amplitude (100% of the pulse magnitude) [19]. Therefore, the PD current pulse expressed by equation (1) is based on the modeling of the traveling waves concept of PD pulses in high voltage cables [15]:

$$V(t) = V_0.(10^{-\alpha t} - 10^{-\beta t}), \tag{1}$$

where $\alpha$ and $\beta$ are time constants parameters related to the cable signal waveform [15]. Thus, considering OHM's Law $I(t) = U(t)/R$ and resistance as 1 Ω, the PD current pulse's initial value was with the magnitude around 200 mA, as described in studies addressing PD pulses [16]. Therefore, the pulse parameters assumed in this paper are: peak at 246 mA, $T_r$ of 0.34435 $\eta s$, $T_f$ =3.2174 $\eta s$, $T_w$ of 1.8503 $\eta s$, $\alpha$ as $7.10^8$, and $\beta$ as $3.10^9$.

### 2.2. Additive white Gaussian noise

In PD analysis the background noise is the signals detected during its onsite measurement. However, external to the DUT [6]. According to the characteristics of time–frequency domain, the disturbances can be classified as white noise (WN), Discrete Spectral Interference (DSI), periodic pulse interference (PPI), stochastic pulse interference (SPI) [20]. Considering PD as pulses of a stochastic and non-stationary nature [21] and that, consequently, the noise acquired in the onsite measurement signal has a random characteristic, it is important to insert the concept of Gaussian Process.

Assuming that the Gaussian process (or random process) is represented by $X(t)$ in the interval of $[0, T]$, with the weight of X(t) over certain function g(t) and integrating the product of g(t)X(t) within that interval, it is expressed as:

$$Y = \int_0^T g(t).X(t)dt, \tag{2}$$

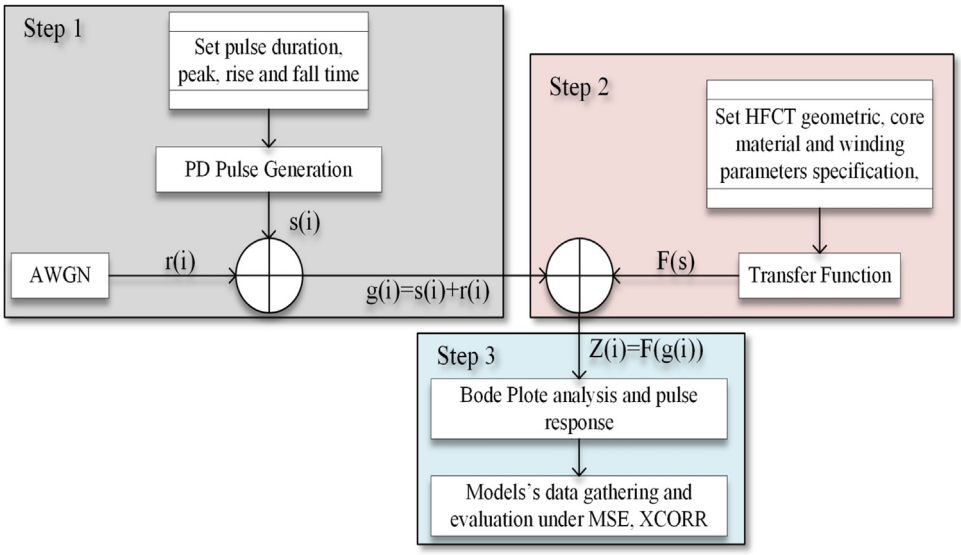


**Fig. 1.** Overall chart flow of the proposed methodology.

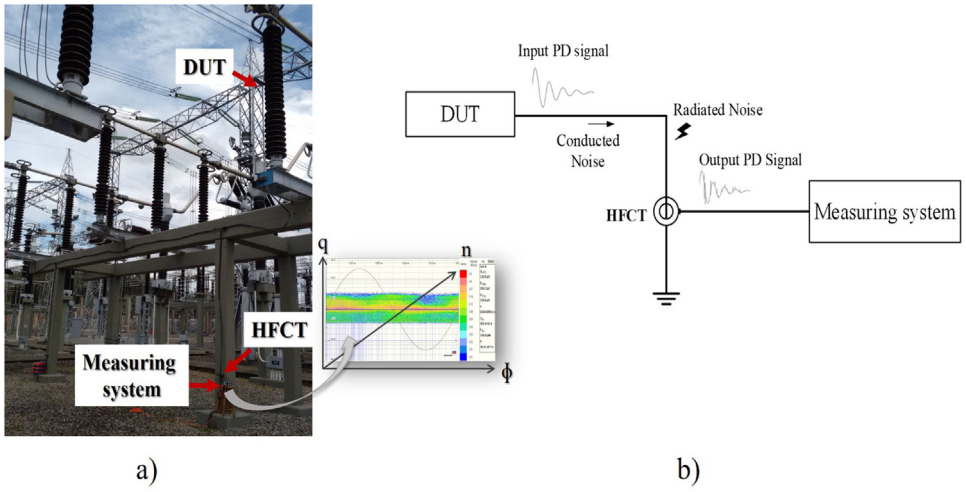


**Fig. 2.** Online measuring of PD by using HFCT: a) Example of onsite PD test; b) Schematic representation of the PD onsite measuring.

in which the mean-square value of $Y$ (linear functional variable of $X(t)$) as finite for certain weighting function $g(t)$, $Y$ is said to be Gaussian-distributed random variable for every $g(t)$ in this class of functions. That is, $X(t)$ is a Gaussian process if every $Y(t)$ is a Gaussian random variable. Then, $Y$ random variable has a Gaussian distribution if its PDF (Probability Density Function) has the form given by Eq. (3):

$$PDF_Y = \frac{1}{\sqrt{2.\pi}.\sigma_Y} \exp\left[-\frac{(Y-\mu_Y)^2}{2\sigma_Y^2}\right], \quad (3)$$

where $\mu_Y$ is the mean, $\sigma_Y$ is the standard deviation, and $\sigma_Y^2$ is the variance of a random $Y$ variable. When the Gaussian random variable $Y$ is normalized to have $\mu_Y$ equals 0 and variance $\sigma_Y^2$ as 1, the normalized Gaussian distribution is commonly written as $N(0.1)$ and the value of the signal will be found in $\pm 3\sigma$ for 99.7% of the considered time interval.

The WN is a kind of Gaussian process, with PSD (Power Spectrum Density) constant regardless of the frequency. Thus, the white Gaussian noise is used as an AWGN of PD from the pulse generator, in order to emulate the on onsite characteristics. Therefore, knowing that the SNR is given by $20.\log_{10} Av_s/Av_n$ [12] – where $Av_s$ represents the input DP signal and $Av_n$ denotes noise – six different conditions of noise. Fig. 3 show the noise condition (PD1 to PD6), from −3dB (harsh environment) to 60 dB (ideal conditions) as well as the respective normalized frequency single side spectrum band (SSB) represented as $|P1(f)|$.

**Table 1**
Classification of the models based on the SNR input levels.

| Label | SNR (dB) | $A_V$ | NoiseAmp |
|---|---|---|---|
| PD1 | −3 | 0.708 | 0.3474576 |
| PD2 | 3 | 1.414 | 0.1739745 |
| PD3 | 6 | 1.995 | 0.1233083 |
| PD4 | 20 | 10 | 0.0246 |
| PD5 | 40 | 100 | 0.00246 |
| PD6 | 60 | 1000 | 0.000246 |

Table 1 shows the input signal 246 mA mixed on 347 mA average signal ($A_V$) for PD1, where the SNR = −3dB in the worse scenario (distorted signal). Whereas, the PD pulse is mixed on ideal noise amplitude in order of $10^-6$ (PD6, SNR = 60 dB) (clean signal). Therefore, the noise level control parameter is the SNR in dB. In this case, the values of signals with AWGN were used as input signals to the HFCT model.

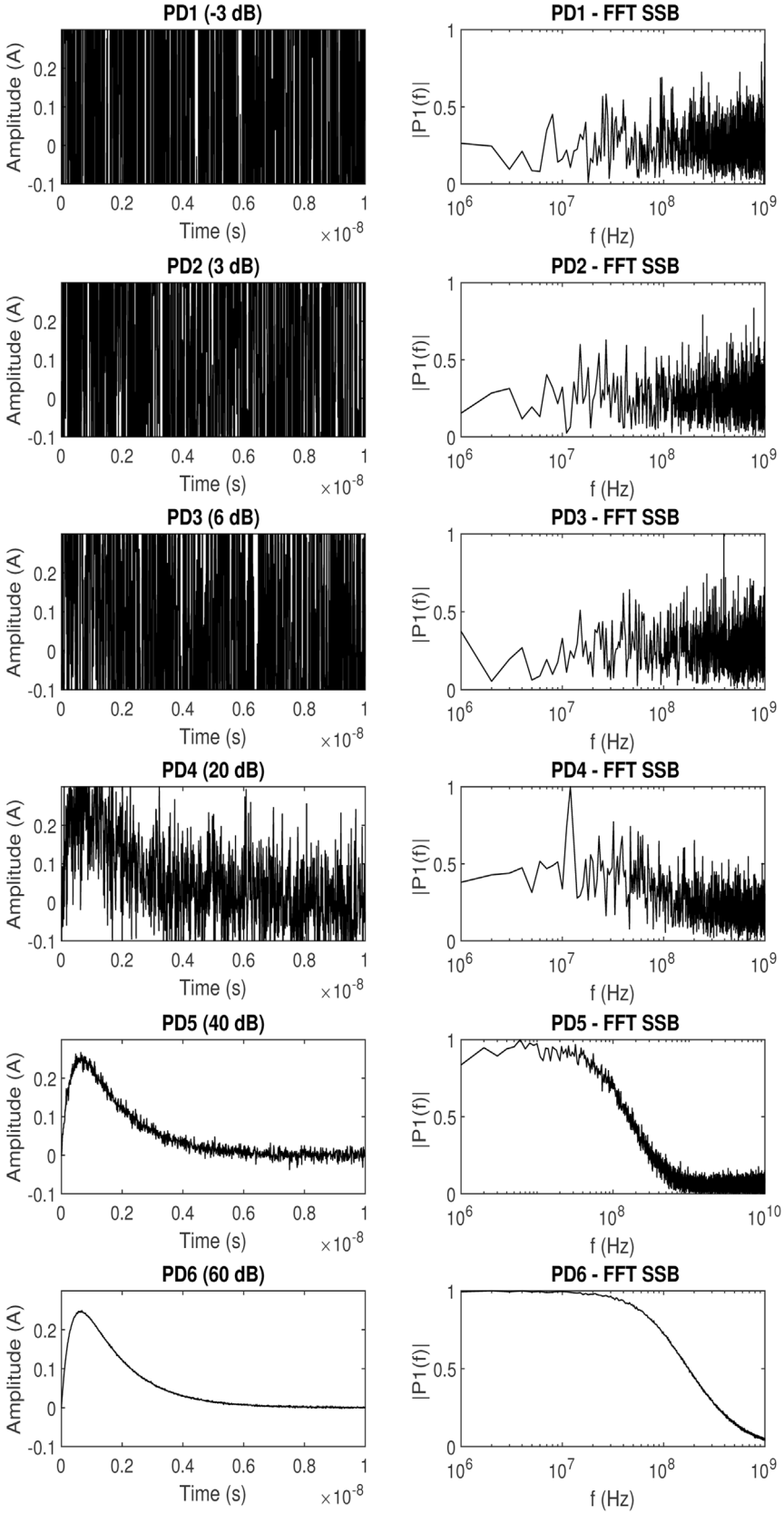


**Fig. 3.** PD pulses generated (left) and their normalized frequency single side spectrum band – SSB (right column).

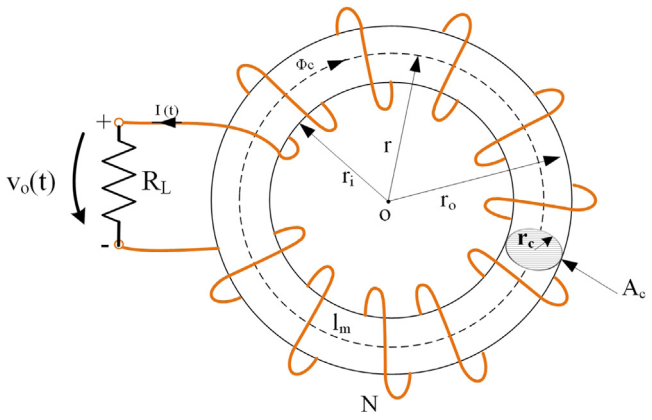


**Fig. 4.** Schematic of the HFCT sensor model.

## 3. HFCT modelling and simulation

The physical geometry parameters of the HFCT sensor is related to a toroidal coil wrapped in a core of high relative permeability. The electrical response of the HFCT sensor is based on the constructive and electrical aspects, given by: geometry, the number of turns, ferromagnetic core material and load resistance (terminal) [22]. Therefore, the dependent characteristics of the HFCT geometry are secondary winding resistance, parasitic capacitance and leakage inductance [22]. The electrical and constructive parameters of the HFCT sensor are highlighted in Fig. 4.

where $R_L$ is the terminal load resistance, $r_i$ is the internal radius, $r_o$ is the external radius, $r$ is the sensor radius (concentric rays at point O), $r_c$ is the radius of the core, $N$ is the number of turns of the sensor coil (secondary circuit), $A_c$ is the cross-sectional area, $l_m$ is the path of the magnetic flux ($\Phi_c$), $I(t)$ is the current of the secondary circuit and $V_o(t)$ is the output voltage of the circuit, i.e., the HFCT sensor output signal.

### 3.1. Constructive aspects based on geometry

The calculation of electrical parameters were carried on considering the references [16,22], and Fig. 4. Therefore, the radius of the HFCT sensor is estimated as, $r = (ri + ro)/2$, the length of flow path is given by, $l_m = 2.\pi.r$ and the radius of the nucleus is given by, $rc = (ro - ri)/2$. The diameter is expressed as $drc = 2.rc$ [m], the cross-sectional area of the core is $A_c = pi.rc^2$ [m$^2$], the length of the winding $pw = rc$ [m] (the length of the winding was used as the same length as $r_c$). The cross sectional area of the coil wire is the same as $A_c$ for convenience (here is used for simulation purpose only), the length of a single coil is $lc = 2.pi.rc$ [m], and the length of the complete coil is $lw = lc.N$ [Nm] (turn.meter).

### 3.2. Electrical parameters

The electrical circuit of the HFCT was analyzed using grouped parameters originating in Fig. 4, and reduced to the electrical scheme shown in Fig. 5 [23].

In addition, the electrical parameters are provided in Table 2. Furthermore, the core material electric and magnetic specification defined as: $\rho$ of $1.6800 \times 10^{-8}$ [Ω.m] (Cooper resistance), $\mu_r$ of 2000 (Relative permeability), $\mu_0$ of $4\pi \times 10^{-7}$ [H/m] (free space permeability), $\mu$ of 0.0025 [H/m] (absolute permeability), $e_0$ of $8.8540 \times 10^{-12}$ [F/m] (free space electric permittivity), and $e_r$ of 1 (relative permittivity),i.e. $e$ is equal to $8.8540 \times 10^{-12}$ [$F/m$] (absolute permittivity). Once the copper resistivity is $\rho = 1.68 \times 10^{-8}$ Ω.m, the winding resistance of the secondary circuit is [16,22]:

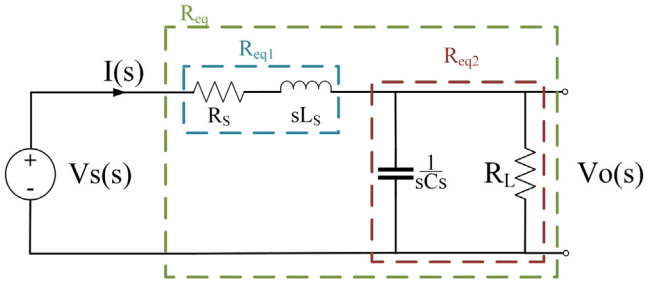


**Fig. 5.** S-domain circuit modeled.

**Table 2**
Modeling constructive parameters used.

| Parameter | Value | Specification |
|---|---|---|
| $d_o$ | 0.1 [m] | Outer diameter |
| $r_0$ | 0.05 [m] | Outer radius |
| $d_i$ | 0.065 [m] | Inner diameter |
| $r_i$ | 0.0325 [m] | Inner radius |
| $N_p$ | 1 | Primary circuit turns |
| $N_s$ | 10 | Secondary circuit turns |
| $d_w$ | 0.0005 [m] | Wire diameter |
| $r_w$ | 0.00025 [m] | Wire radius |
| $A_c$ | $2.4053 \times 10^{-4}$ [m$^2$] | Core area |
| $r_c$ | 0.0088 [m] | Care radius |
| $dr_c$ | 0.0175 [m] | Core diameter |
| $r$ | 0.0575 [m] | Sensor radius |
| $l_m$ | 0.3613 [m] | Flux path |
| $A_w$ | $2.4053 \times 10^{-4}$ [m$^2$] | Coil cross-section area |
| $l_c$ | 0.0550 [m] | One turn length |
| $p_w$ | 0.0088 [m] | Coil step back |

$$Rs = \frac{\rho.l_w}{A_w}. \tag{4}$$

The secondary sensor voltage is expressed as:

$$v_s(t) = -M_c.\frac{di_p(t)}{dt}. \tag{5}$$

Mutual inductance is given by [16]:

$$M_c = \frac{N_s^2.\mu.A_c}{l_m}, \tag{6}$$

where $\mu$ is given by $\mu = \mu_r \cdot \mu_o$, in which $\mu_r$ is the relative permeability (value according to the material) and $\mu_o$ is the vacuum permeability with the value of $4\pi 10^{-7}$ H/m. The $N_s$ is the number of turns of the secondary, i.e. winding of the sensor. In leakage inductance (also called auto-inductance) [24], the circular coil method was used for single turn inductance and for $rw \ll rc$, thus, based on:

$$Lloop = \mu_0.r_c.\log_{10}\left[\left(\frac{8.r_c}{r_w}\right) - 2\right]. \tag{7}$$

The resulting leakage inductance for the entire coil is:

$$Ls = N_s^2.L_{loop}. \tag{8}$$

Since the application is in HF, the value of the parasitic capacitance ($Cs$) of the secondary winding must be estimated. The parasitic effect was estimated using the analytical approach of [24], in which: $e_0 = 8.854.10^-12$ (dielectric constant), $e_r = 1$ (relative permittivity of air) and $e = e_0 e_r$ (absolute permittivity), therefore:

$$Cs = \frac{lw.pi.e}{acosh\left(\frac{pw}{2.r_w}\right)}. \tag{9}$$

**Table 3**
Specification of the electrical components for each model.

| Group | Model | Specification |
|---|---|---|
| Reference | PAD | $R_L = 50$, $N_s = 10$, $\mu_r = 2000$ |
| | N30 | $R_L = 50$, $N_s = 30$, $\mu_r = 2000$ |
| Variation | RL250 | $R_L = 250$, $N_s = 10$, $\mu_r = 2000$ |
| | mur2300 | $R_L = 50$, $N_s = 10$, $\mu_r = 2300$ |
| | RLNmur | $R_L = 150$, $N_s = 20$, $\mu_r = 2100$ |

Although *Ls* and *Cs* are intrinsic to the HFCT sensor, requiring the calculation of the capacitive network and experimental calculation of the HFCT sensor dimensions, as demonstrated by [24]. This paper is restricted to the analytical calculation of *Cs* and *Ls* since such parameters are not the present study's initial objective. Despite this, the values obtained in this study were consistent with [25].

Therefore, the final proposal TF considering the second-order polynomial expressed by equation (10) is:

$$F(s) = \frac{\frac{-sMc.Np.R_L}{Cs.R_L.(Ls+Mc).Ns}}{s^2 + s\left(\frac{Cs.R_L.R_s+Ls+Mc}{Cs.R_L.(Ls+Mc)}\right) + \frac{R_s+R_L}{Cs.R_L.(Ls+Mc)}}. \quad (10)$$

The frequency resonance ($w_0$) in $rad/s$:

$$w_0 = \sqrt{\frac{R_L}{Cs.R_L.(Ls+Mc)}}. \quad (11)$$

Also, the damping coefficient ($\zeta$), given b:

$$\zeta = \frac{(Cs.R_L.R_s + Ls + Mc)\sqrt{Cs.R_L.(Ls+Mc)}}{2.Cs.R_L(Ls+Mc)\sqrt{R_L}}. \quad (12)$$

The values of $w_0$ and $\zeta$ provide data for system behavior since: $\zeta > 1$ provides a overdamped response (real and different roots and product of two 1st-order poles); $\zeta < 1$ determine a underdamped response (complex roots) of the system; $\zeta = 1$ results in critically damped response (real and equal roots). Thus, Fig. 4 can be modeled according to Fig. 5 in the *s* domain. Note that $R_{eq1}$ and $R_{eq2}$ are equivalent resistances from resistive associations in series (between $R_s$ and $sL_s$) and in parallel (between $1/sCs$ and $R_L$), respectively and whose total equivalent resistance is $R_{eq}$ (series association between $R_{eq1}$ and $R_{eq2}$).

### 3.3. Simulation

In order to assess the hypothesis of improvement or deterioration of the HFCT signal response, we consider the S-domain through a transfer function optimization, which means the frequency response. Five different models have been settled as described in Table 3, which were divided into reference and variation groups. The reference model (PAD) is the standard model, whereas $R_L$ (load resistance), $N_s$ (number of secondary turns) and $\mu_r$ (relative permeability) are variation models. On the other hand, the variation models called N30, RL250, mur2300 and RLNmur were organized to test the general performance of the HFCT sensor, with changes in its parameters based on the PAD.

The five TFs, considering the calculations based on the specified parameters in Table 3, are presented in Table 4.

The Bode diagram was considered (Fig. 6), to obtain the frequency response of the HFCT sensor models, through simulation with Matlab software.

Also, in Fig. 6, the frequency response allowed the analysis of magnitude data (dB) and phase (degrees) in the frequency domain. Tables 5 and 6 shows the physical and electrical parameters, respectively, calculated and obtained for all the models (PAD, N30, RL250, mur2300, and RLNmur), through simulation with Matlab software.

**Table 4**
Models transfer functions.

| Model | Transfer function |
|---|---|
| PAD | $F(s) = \frac{-2.27\times10^{10}s}{s^2+4.649\times10^9 s+1.357\times10^{15}}$ |
| N30 | $F(s) = \frac{-0.00251s}{9.95^{-13}s^2+0.001542s+50}$ |
| RL250 | $F(s) = \frac{-0.004183s}{1.843^{-13}s^2+0.0001713s+250}$ |
| mur2300 | $F(s) = \frac{-0.0009621s}{4.225^{-14}s^2+0.0001964s+50}$ |
| RLNmur | $F(s) = \frac{-0.005271s}{9.277^{-13}s^2+0.0007187s+150}$ |

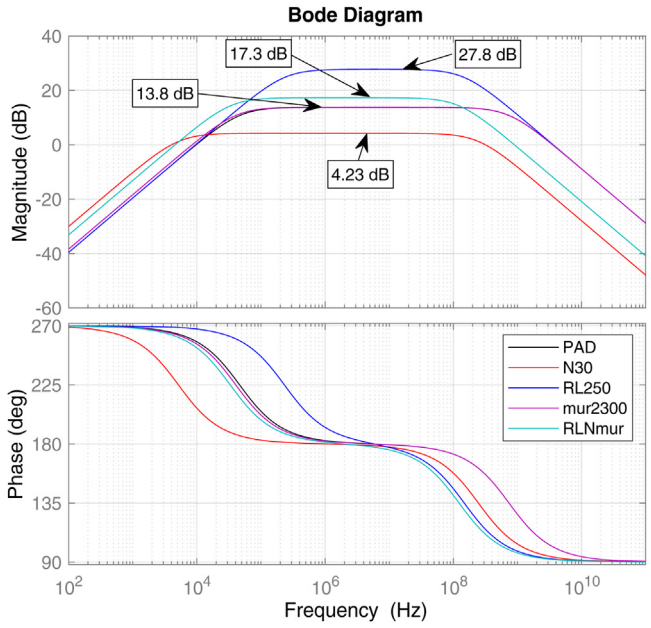


**Fig. 6.** Frequency response of the HFCT sensor models.

**Table 5**
Performance based on the physical parameters obtained for each model.

| Model | Poles | $\zeta$ | BW (Hz) |
|---|---|---|---|
| PAD | $s_1 = -2.92E+05$<br>$s_2 = -4.65E+09$ | 6.3104E+01 | 5.03E+09 |
| N30 | $s_1 = -3.24E+04$<br>$s_2 = -1.55E+09$ | 1.0930E+02 | 4.89E+08 |
| RL250 | $s_1 = -1.46E+06$<br>$s_2 = -9.28E+08$ | 1.2621E+01 | 1.32E+09 |
| mur2300 | $s_1 = -2.55E+05$<br>$s_2 = -4.65E+09$ | 6.7569E+01 | 4.95E+09 |
| RLNmur | $s_1 = -2.09E+05$<br>$s_2 = -7.75E+08$ | 3.0465E+01 | 1.32E+09 |

**Table 6**
Electrical stray parameters obtained for the models.

| Model | $R_s(\Omega)$ | *Ls* (H) | *Cs* (F) |
|---|---|---|---|
| PAD | 3.84E-05 | 4.00E-06 | 4.30E-12 |
| N30 | 1.15E-04 | 3.60E-05 | 1.29E-11 |
| RL250 | 3.84E-05 | 4.00E-06 | 4.30E-12 |
| mur2300 | 3.84E-05 | 4.00E-06 | 4.30E-12 |
| RLNmur | 7.68E-05 | 1.60E-05 | 8.60E-12 |

The PAD's gain reaches 13.8 dB (Fig. 6), and in the resonance frequency, there is a 180° phase shift, according to Lenz's Law. In the case of variation models (N30, RL250, mur2300, and RLNmur), which are described in Tables 5 and 6 . Since the size of the core ($r_i$, $r_o$, $r$, and $r_c$) was maintained, and the $R_L$, $N_s$ and $\mu_r$ were altered (Table 3), distinct performances were obtained between the HFCT sensor models.

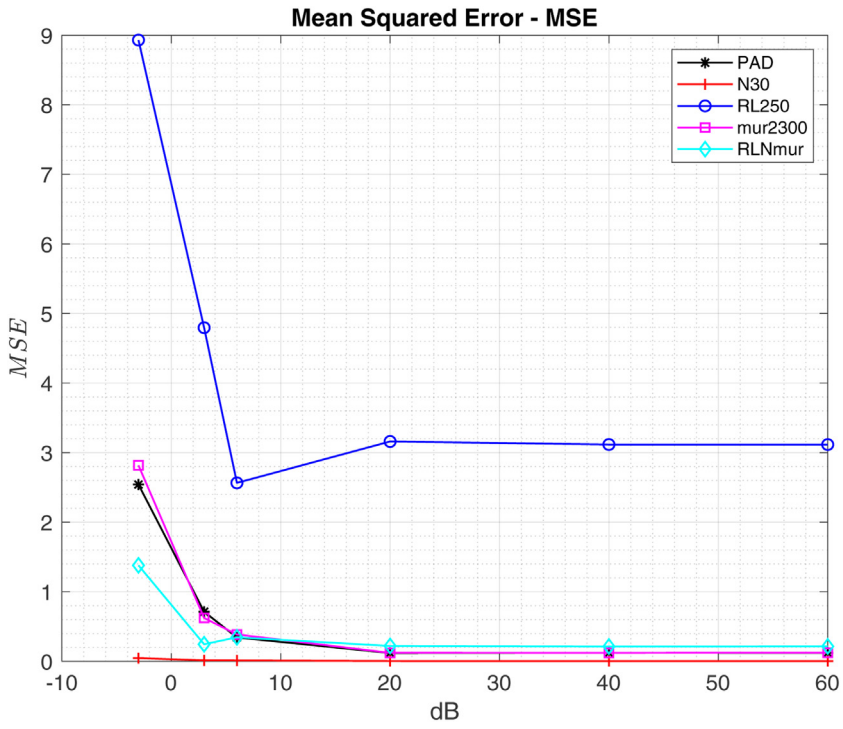


**Fig. 7.** MSE of the HFCT sensor models.

The Bode diagram (Fig. 6), shows that the N30's gain reaches 4.23 dB. Also, Table 5 presents the smoothest response due to the increase in the $\zeta$ to 1.0930E+02. In addition, also in the Bode diagram (Fig. 6), there is a flatter curve at the center of phase charge attributed to the increase (higher winding turns) in the reactive characteristics of the *Cs* and *Ls* in relation to the PAD.

Unlike model N30, the model RL250 has a direct change in the $R_L$, i.e., non-reactive electrical parameter. Comparatively to PAD, the Bode diagram (Fig. 6), shows the higher gain (27.8 dB). Consequently, Table 5 shows the RL250 response results in a wider bandwidth, BW = $1.32E + 09$ Hz, and decreasing on $\zeta = 1.2621E + 01$.

In the mur2300, the $\mu_r = 2300$, based on [26], and based on the Bode diagram (Fig. 6), it is observed that the gain is 13.8 dB. The characteristic response of mur2300 is almost the same for PAD, once changing $\mu_r$ (Table 3) does not change the reactive parameters (Tables 5 and 6). Thus, this ends up causing an overlapping in the PAD response curve (Fig. 6).

The RLNmur's gain reaches 17.3 dB in the Bode diagram (Fig. 6), corresponding to the intermediate response between the PAD, mur2300, and RL250 models, regarding the characteristics of the reactive parameters.

## 4. HFCT performance evaluation

Based on the simulation results presented in Section 3.3, It has been considered a decrease in magnitude and an increase in BW with increased windings in the secondary circuit (model N30). In the model N30, there is a phase advance concerning frequency. Also, it was found that increasing the value of $\mu_r$, in the case of mur2300, did not lead to a considerable change in magnitude and phase response, compared to PAD. However, to complement the HFCT performance evaluation analysis, the mean squared error (MSE) and cross-relation (XCORR) were considered.

### 4.1. Data analysis evaluation metrics

Two metrics has been used in this paper, the MSE and XCORR, between signals obtained ($Z(i)$) and the input signals ($s(i)$) (refer to Fig. 1). The MSE is given by [12]:

$$MSE = \frac{1}{N}\sum_{i=1}^{N}|z(i) - s(i)|^2. \tag{13}$$

The MSE is generally used to assess the degree of distortion caused by removing noise from a signal, so the lower the MSE value, the smaller the error. In contrast, the XCORR coefficient ($\rho_{sz}$) is expressed by [12]:

$$\rho_{sz}(n) = \sum_{i=0}^{N-n-1} s(i).z(i+n). \tag{14}$$

The XCORR coefficient assesses the similarity in the shape of the signals' wave; it was normalized in order that a zero XCORR factor indicates total asymmetry while an XCORR factor of 1 indicates complete symmetry. Therefore, the XCORR is applied between the $Z(i)$ and $s(i)$ (see Fig. 1) on discrete-time. Also, since this Eq. (14) returns a vector, the sequences of the XCORR have been normalized.

The MSE obtained for all HFCT sensor models it is expressed in Fig. 7. The MSE for the RL250 model (Fig. 7) is the greatest one. On the other hand, increasing the number of windings (N30 model), the similarity between the $s(i)$ and the $Z(i)$ (HFCT sensor response) increases, given that the mutual inductance is the highest among the models, $M_c = 1.5$ mH, while in the PAD model the mutual inductance is $M_c = 0.17$ mH, i.e., an increase of 20 in the number of turns of the winding results in an increase of 8.82 times the value of $M_c$ (see Eq. (6)). Furthermore, it has been observed that from SNR = 6 dB, the MSE remains below 1 for all the models excepting RL250. Therefore, in the case of PAD, N30, mur2300, and RLNmur the $Z(i)$ must be at least 2 twice the $s(i)$ to reach an acceptable measurement error.

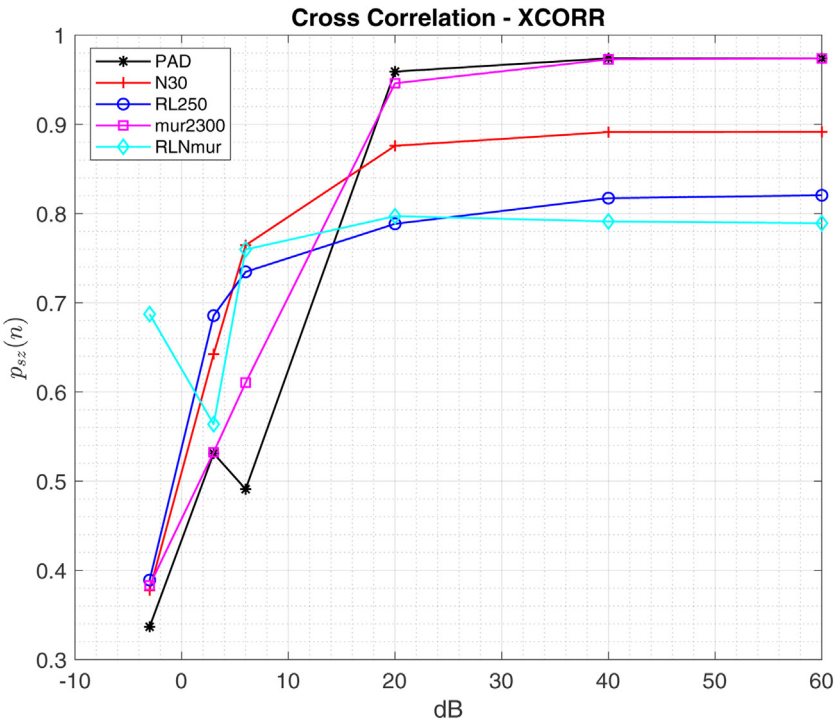


**Fig. 8.** XCORR of the HFCT sensor models.

The XCORR obtained for all HFCT sensor models it is expressed in Fig. 8. The XCORR analysis (Fig. 8) reinforces that the TFs modeled for HFCT sensor models, provides a good performance for an SNR above 6 dB (Fig. 7), and XCORR coefficient values upper 0.5 (e.g. 0.7645 for N30 model).

## 5. Conclusions and prospects

This paper addressed the physical effects, modelling, and simulation of the high-frequency current transformer (HFCT), applied to time measurements of the partial discharges (PD) under the strong influence of background noises.

Several factors limit the frequency responses of the N30, RL250, mur2300, and RLNmur models. In the real HFCT sensor, the frequency response entails several parameters. The main ones being reactive components with origin in construction and electrical phenomena since a coil has (i) capacitance and (ii) inductance, due to the association of turns. Hence, these reactive components contribute to self-capacitance and self-inductance, respectively. However, state-of-the-art studies describe that the load resistance value must be 50 Ω, due to the resistive coupling with the measuring instruments, to eliminate losses. The present paper employs a variation of up to 250 Ω to verify changes in response to the input signal and performance evaluation under noisy conditions.

Thus, the hypothesis of improvement or deterioration of the HFCT signal response, through a transfer function optimization, for an eventual redefinition of physical and geometrical parameters of the HFCT sensor, can be validated, depending on which parameters are chosen to be changed. Additionally, the HFCT model N30 provided more reliable S-domain values by increasing the number of coil turns adaptively to the noisy signal compared to the other models analyzed, i.e., RL250, mur2300, and RLNmur.

Therefore, the proposed transfer function optimization approach gives a robust pre-processing by changing the features of the HFCT's electrical circuit and coil construction parameters to reach a high signal-to-noise (SNR) ratio. Furthermore, this paper serves as an inspiration for potential solutions through artificial intelligence. In this way, it is possible to optimize the electrical parameters to obtain ideal characteristics of magnitude and phase in the frequency response to reject different characteristic field noise (onsite measurement).

## CRediT authorship contribution statement

**Douglas Nascimento**: Conceptualization, Methodology, Investigation, Data curation, Validation, Formal Analysis, Writing – original draft. **Shady S. Refaat**: Writing – review & editing, Resources, Project administration, Funding acquisition. **Hermes Loschi**: Data curation, Visualization, Methodology, Writing – Original draft, Writing – review & editing. **Yuzo Iano**: Supervision, Writing – review & editing. **Euclides Chuma**: Writing – review & editing. **Waseem El-Sayed**: Writing – review & editing. **Amr Madi**: Writing - review & editing.

## References

[1] D.A. Nascimento, Y. Iano, H.J. Loschi, L.A.S. Ferreira, J.A.D. Rossi, C.D. Pessoa, Evaluation of partial discharge signatures using inductive coupling at on-site measuring for instrument transformers, Int. J. Emerging Electric Power Syst. 19 (1) (2018), http://dx.doi.org/10.1515/ijeeps-2017-0160.

[2] D.A. Nascimento, S.S. Refaat, A. Darwish, Q. Khan, H. Abu-Rub, Y. Iano, Investigation of void size and location on partial discharge activity in high voltage XLPE cable insulation., in: In WCNPS 2019 - Workshop on Communication Networks and Power Systems, number Wcnps. IEEE. ISBN 9781728129204. doi:10.1109/WCNPS.2019.8896268, 2019, pp. 1–6.

[3] G.C. Montanari, A. Cavallini, Insulation condition assessment of power equipments in electrical assets based on on-line monitoring of partial discharges, in: In 2008 International Conference on Condition Monitoring and Diagnosis. IEEE, ISBN 9781424416219. doi:10.1109/CMD.2008.4580483, 2007, pp. 7–12.

[4] V. Estrela, Os. Saotome, H. Loschi, J. Hemanth, W. Farfan, J. Aroma, C. Saravanan, E. Grata, Emergency response cyber-physical framework for landslide avoidance with sustainable electronics †, Technologies 6 (2) (2018) 42, 2227-7080. doi:10.3390/technologies6020042.

[5] A. Cavallini, G.C. Montanari, A. Contin, F. Puletti, A new approach to the diagnosis of solid insulation systems based on PD signal inference, IEEE Electr.

Insulation Mag. 19 (2) (2003) 23–30, http://dx.doi.org/10.1109/MEI.2003.1192033.
[6] IEC. IEC 60270- High-voltage test techniques - Partial discharge measurements Techniques. Technical Report 40, 2015.
[7] F. Álvarez, F. Garnacho, J. Ortego, M.A. Sánchez-Urán, Application of HFCT and UHF sensors in on-line partial discharge measurements for insulation diagnosis of high voltage equipment, Sensors (Switzerland) 15 (4) (2015) 7360–7387, http://dx.doi.org/10.3390/s150407360.
[8] IEC, IEC TS 62478 - High voltage test techniques - Measurement of partial discharges by electromagnetic and acoustic methods. Technical report, IEC, 2016.
[9] E. Gulski, W. Koltunowicz, T. Ariaans, G. Behrmann, R. Jongen, F. Garnacho, S. Kornhuber, S. Ohtsuka, F. Petzold, M. Sanchez-Uran, K. Siodla, S. Tenbohlen, Guidelines for partial discharge detection using conventional (IEC 60270) and unconventional methods. Technical Report 288, Cigré, 2016.
[10] A. Martins, V.V. Estrela, EM-based mixture models applied to video event detection, Principal Component Analysis - Engineering Applications (2012), http://dx.doi.org/10.5772/38129.
[11] A.M. Coelho, V.V. Estrela, F.P. Carmo, S.R. Fernandes, Error concealment by means of motion refinement and regularized Bregman divergence., in: In Lecture Notes in Computer Science (including subseries Lecture Notes in Artificial Intelligence and Lecture Notes in Bioinformatics), volume 7435 LNCS ISBN 9783642326387. doi:10.1007/978-3-642-32639-4_78, 2012, pp. 650–657.
[12] R. Hussein, K.B. Shaban, A.H. El-Hag, Denoising different types of acoustic partial discharge signals using power spectral subtraction, High Voltage 3 (1) (2018) 44–50, 2397-7264. doi:10.1049/hve.2017.0119. URL http://digital-library.theiet.org/content/journals/10.1049/hve.2017.0119.
[13] R. Hussein, A.H. El-Hag, K.B. Shaban, Energy conservation-based thresholding for effective wavelet denoising of partial discharge signals, IET Science, Measurement & Technology 10 (7) (2016) 813–822, 1751-8822. doi:10.1049/iet-smt.2016.0168. URL http://digital-library.theiet.org/content/journals/10.1049/iet-smt.2016.0168.
[14] C. Zachariades, R. Shuttleworth, R. Giussani, R. Mackinlay, Optimization of a high-frequency current transformer sensor for partial discharge detection using finite-element analysis, IEEE Sensors J. 16 (20) (2016) 7526–7533, http://dx.doi.org/10.1109/JSEN.2016.2600272.
[15] H.A. Illias, H.R. Yon, A.H.A. Bakar, H. Mokhlis, G. Chen, P.L. Lewin, A.M. Ariffin, Modelling of partial discharge pulses in high voltage cable insulation using finite element analysis software, in: 2013 IEEE Electrical Insulation Conference, EIC 2013, (June), doi:10.1109/EIC.2013.6554201, 2013, pp. 52–56.
[16] X. Hu, W.H. Siew, M.D. Judd, X. Peng, Transfer function characterization for HFCTs used in partial discharge detection, IEEE Transactions on Dielectrics and Electrical Insulation 24 (2) (2017) 1088–1096, http://dx.doi.org/10.1109/TDEI.2017.006115.
[17] Yasin Khan, Partial discharge pattern analysis using PCA and back-propagation artificial neural network for the estimation of size and position of metallic particle adhering to spacer in GIS, Electrical Engineering 98 (2016) 29–42, doi:10.1007/s00202-015-0343-4. URL https://link.springer.com/article/10.1007/s00202-015-0343-4.
[18] Jankauskas Audrius Liudas, Rekuviene Regina Samaitis, Vykintas Mažeika, Detection and localization of partial discharge in connectors of air power lines by means of ultrasonic measurements and artificial intelligence models, Sensors 20 (2021) 1–21, doi:10.3390/s21010020. URL https://www.mdpi.com/1424-8220/21/1/20#.
[19] M. Wu, H. Cao, J. Cao, H.L. Nguyen, J.B. Gomes, S.P. Krishnaswamy, An overview of state-of-the-art partial discharge analysis techniques for condition monitoring, IEEE Electr. Insulation Mag. 31 (6) (2015) 22–35, http://dx.doi.org/10.1109/MEI.2015.7303259.
[20] L. Satish, B. Nazneen, Wavelet-based denoising of partial discharge signals buried in excessive noise and interference, IEEE Trans. Dielectr. Electr. Insul. 10 (2) (2003) 354–367, http://dx.doi.org/10.1109/TDEI.2003.1194122.
[21] A.L. Kupershtokh, D.I. Karpov, D.A. Medvedev, C.P. Stamatelatos, V.P. Charalambakos, E.C. Pyrgioti, D.P. Agoris, Stochastic models of partial discharge activity in solid and liquid dielectrics, IET Sci. Measure. Technol. 43 (3) (2007) 303–311, http://dx.doi.org/10.1049/iet-smt:20060104.
[22] A.K.A. Hagh, S.J. Ashtiani, A.A. Shayegani Akmal, A wideband, sensitive current sensor employing transimpedance amplifier as interface to Rogowski coil, Sensors and Actuators, A: Physical 256 (2017) 43–50, 09244247. doi:10.1016/j.sna.2017.01.018. URL https://doi.org/10.1016/j.sna.2017.01.018.
[23] M.H. Samimi, Arash Mahari, M.A. Farahnakian, H. Mohseni, The rogowski coil principles and applications: A review, IEEE Sensors Journal 15 (2) (2015) 651–658, http://dx.doi.org/10.1109/JSEN.2014.2362940.
[24] L. Kütt, Analysis and Development of Inductive Current Sensor for Power Line On-Line Measurements of Fast Transients. PhD thesis, 2012.
[25] B.Mi. Amna, U. Khayam, Design and Simulation of High Frequency Current Transformer as Partial Discharge Detector., in: In The 3rd IEEE Conference on Power Engineering and Renewable Energy ICPERE 2016, ISBN 9781509051083. doi:10.1109/ICPERE.2016.7904854, 2016, pp. 135–139.
[26] M.E. Kiziroglou, S.W. Wright, E.M. Yeatman, Coil and core design for inductive energy receivers, Sens. Actuators A: Phys. 313 (2020) 112206, 09244247. doi:10.1016/j.sna.2020.112206. URL https://doi.org/10.1016/j.sna.2020.112206.

## Biographies

**Douglas Nascimento, M.Sc.,** received his B.Sc. at University of West Santa Catarina and M.Sc. in Electrical Engineering from the University of Campinas. Currently is a Ph.D. candidate and Early Stage Researcher in the ETOPIA (European Training Network of PhD Researchers on Innovative EMI Analysis and Power Applications) Project, a joint doctoral programme under The European Commission Horizon 2020 initiative, Marie Skłodowska-Curie Actions, at The University of Zielona Góra and at The University of Twente. He is a member of Institute of Electrical and Electronic Engineers (IEEE), and Electromagnetic Compatibility Society (EMC-S) working on TC-7 (Technical Committee). His research areas address electric vehicles, smart cities, sensors, EMC and EMI. He has experience in electromagnetic modeling, cable and sensor design, simulation of electric circuits, and partial discharge tests.

**Shady S. Reffat, Ph.D.,** is a postdoctoral research associate in the Department of Electrical and Computer Engineering, Texas A&M University at Qatar, a member of the Institute of Electrical and Electronic Engineers (IEEE), a member of The Institution of Engineering and Technology (IET), a member of the Smart Grid Center – Extension in Qatar (SGC-Q), he has worked with industry for over fifteen years as electrical design engineer. He has published over twenty journal and conference papers. His research interests include electrical machines, power system, smart grid, energy management system, reliability of power grid and electric machinery, fault detection, and condition monitoring in conjunction with fault management and development of fault tolerant systems. He has successfully realized many potential research projects.

**Hermes Loschi, M.Sc.,** was born in 1990, Sao Paulo, Brazil. He received his master degree in Electrical Engineering at the University of Campinas and his bachelor's degree in Control and Automation Engineering at the Paulista University. Since April 2019, he started as a Ph.D. student in "Smart Cities EMC Network for Training (SCENT)" project in the Institute of Automatic Control, Electronics and Electrical Engineering at the University of Zielona Gora, Poland as well as the faculty of Electrical Engineering, Mathematics and Computer Science (EEMCS) in the University of Twente, Netherlands. His research areas are power systems, renewable energies, sensors, EMC and EMI.

**Yuzo Iano, Prof. Ph.D.,** has a degree (1972), a master's degree (1974) and a doctorate (1986) in Electrical Engineering from the University of Campinas (Unicamp). Since then, he was a supervisor in 5 postdoctoral projects, 34 doctoral theses, 59 master's dissertations, 74 undergraduate studies, 48 undergraduate research, and 198 other orientations (Teacher Internship Program, projects, etc.). Author of 2 books and author/co-author of 8 book chapters, and 300 published articles. He received two Innovation Awards, Category "Licensed Technology", from Inova Unicamp in the years 2013 and 2018, an Award for Teaching Excellence in Undergraduate Education, from the Faculty of Electrical and Computer Engineering, from the University of Campinas (2012) and a "Life Member" honor granted by the International Institute of Electrical and Electronics Engineers - IEEE (2018). He is currently Full Professor MS6 in RDIDP of Decom/Feec/Unicamp.

**Euclides Chuma, Ph.D.,** is currently R&D Manager of Photonics Innovation Institute. He completed his degree in Mathematics from the University of Campinas (UNICAMP) (2003), graduate degree in Network and Telecommunications Systems from INATEL (2015), MSc in Electrical Engineering from UNICAMP (2017), and PhD in Electrical Engineering in UNICAMP (2019). His research interests include antennas, microwave, millimeter wave, photonics, sensors, wireless power transfer, and softwaredefined radio.

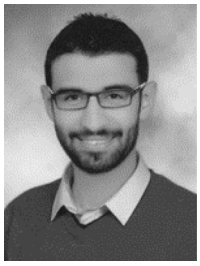

**Waseem El Sayed, M.Sc.,** Was born in 1991, in Alexandria, Egypt. He finished his B.Sc. and M.Sc. studies in electrical and control engineering from the Arab Academy for Science and Technology and Maritime Transport (AASTMT), Egypt in 2013, and 2018 respectively. In April 2019, he started his Ph.D. studies as Earlier Stage Researcher number 1 in the "SCENT - Smart Cities EMC Network for Training" project, he recruited as a Ph.D. student in the Institute of Automatic Control, Electronics and Electrical Engineering at the University of Zielona Gora, Poland as well as the faculty of Electrical Engineering, Mathematics and Computer Science (EEMCS) in the University of Twente, Netherlands.

**Amr Madi, M.Sc.** is a M.Sc, Electrical Engineer, and Early Stage Researcher in the joint doctoral programme under The European Commission Horizon 2020 initiative, Marie Skłodowska-Curie Actions, at the University of Zielona Góra. His research areas are power systems, sensors, EMC, and EMI, Smart grid, Power quality, Power electronics, Renewable Energy, Environmental Engineering, Climate change, and WasteWater management.